Monte Carlo study of the *XY* vector Blume-Emery-Griffiths model for ^{3}He—^{4}He mixtures in three dimensions

R. T. S. Freire,[1,2,*] S. J. Mitchell,[1,†] J. A. Plascak,[1,2,‡] and D. P. Landau[1,§]
[1]*Center for Simulational Physics, University of Georgia, Athens, GA 30602, USA*
[2]*Departamento de Física-ICEx, Universidade Federal de Minas Gerais Caixa Postal 702, 30123-970 Belo Horizonte, MG, Brasil*
(Received 6 July 2005; published 15 November 2005)

A version of the Vector Blume-Emery-Griffiths model with three-dimensional spins was studied on a simple cubic lattice by Monte Carlo simulations. We obtained the phase diagram, which reproduces, for a range of the parameters of the model, the topology of the one observed for bulk mixtures of ^{3}He—^{4}He. The phase diagram displays a superfluid, ^{4}He-rich phase which undergoes a phase transition to a normal phase. This transition is first or second order, depending on the region of the phase diagram examined. One of the main features of this diagram is the existence of a tricritical point, which, for some values of the parameters of the model, decomposes into a critical endpoint and a double critical endpoint. These points were located with reasonable precision. This study provides the basis for the subsequent study of dynamic properties of ^{3}He—^{4}He mixtures.

DOI: 10.1103/PhysRevE.72.056117 PACS number(s): 05.50.+q, 67.60.−g, 64.60.Cn, 64.60.Kw

I. INTRODUCTION

The nature of phase transitions in superfluid helium has long been a topic of intense investigation. This is due especially to its unusual characteristics which permit transitions to be studied with high resolution and with no complexities arising from impurities and crystalline imperfections. One remaining limitation was gravity, but with experiments conducted in microgravity conditions, new data could be obtained with unparalleled resolution [1].

It has long been recognized that the *XY* model of magnetism should be in the same universality class of liquid ^{4}He and so suitable for the study of the superfluid phase transition [2]. Recently much interest has been given to the study of dynamic properties of the *XY* model in the bulk and in confined geometries. For instance, studying the transport properties of the model near criticality, it is possible to relate them to the thermal conductivity of superfluid ^{4}He, which is an experimentally accessible quantity [3,4].

Another interesting class of systems are ^{3}He—^{4}He mixtures, where ^{3}He atoms act as impurities which reduce the superfluid transition temperature and drives the system towards phase separation [5,6]. In 1971, Blume, Emery and Griffiths [7] proposed a simple discrete spin model which could mimic the basic features of the bulk phase diagram of ^{3}He—^{4}He mixtures, although it carried some unphysical properties, as not considering the rotational symmetry of the superfluid order parameter (the wave function of superfluid helium). The model was solved in the mean field approximation and for reasonable values of the parameters the model qualitatively reproduced the experimental phase diagram, including the tricritical point. Berker and Nelson [8], and independently Cardy and Scalapino [9], proposed a planar rotator model to account for the behavior of films of ^{3}He—^{4}He mixtures, known as the vector Blume-Emery-Griffiths (VBEG) model. The bulk phase diagram of the model was investigated in two dimensions using the Migdal-Kadanoff recursion relations and no tricritical point was found for any values of the parameters. More recently, Maciolek *et al.* [10] studied the phase diagram of the planar-rotator VBEG model in the bulk in three dimensions by the molecular field approximation and Monte Carlo simulations; however, the model does not possess intrinsic spin dynamics (the spins are two dimensional) and is therefore not suitable for future work regarding dynamic properties of the system. Thus, our purpose here is to study the phase diagram of the *XY* VBEG model (which presents three-dimensional spins and, therefore, intrinsic spin dynamics) by Monte Carlo simulations.

The model is defined in Sec. II. In Sec. III we give the details of the simulational methods, and the results are presented in Sec. IV. The conclusions are given in the last section.

II. THE MODEL

The system was simulated on a simple cubic lattice and the hamiltonian is defined by an *XY* model embedded in a lattice-gas model

$$H = -J\sum_{\langle i,j\rangle}[S_i^x S_j^x + S_i^y S_j^y] - K\sum_{\langle i,j\rangle} S_i^2 S_j^2 + \Delta\sum_i (S_i)^2, \quad (1)$$

where $\vec{S}$ represents a three-dimensional classical spin, the first two sums are over nearest-neighbor pairs $\langle i,j\rangle$ and the last one is over all sites i of the lattice. In this work, $J=1$. There are two kinds of particles in the system—magnetic (spin 1) and nonmagnetic (spin zero) particles. Magnetic particles represent ^{4}He atoms and the spin orientation accounts for the internal superfluid degrees of freedom. Nonmagnetic particles represents ^{3}He atoms. The first term in the Hamiltonian accounts for superfluidity, while the second term

*Electronic address: rfeire@fisica.ufmg.br
†Electronic address: smitchell@hal.physast.uga.edu
‡Electronic address: pla@fisica.ufmg.br
§Electronic address: dlandau@hal.physast.uga.edu

 ©2005 The American Physical Society

arises from a phenomenological modeling of the interaction energy between pairs of helium particles of the same or different species. The parameter Δ is essentially the chemical potential difference $\mu_3 - \mu_4$ of ^{3}He and ^{4}He, respectively. More details about the model can be found in Refs. [7,10].

III. SIMULATIONAL METHODS

In order to explore the phase space of the model, we used (i) lattice-gas moves combined with (ii) spin-reorientation updates. The lattice-gas moves account for the phase separation in our model. The spin reorientation updates are related to the long-range magnetic order, which corresponds to the superfluid phase. We also applied a nonergodic version of the Wolff algorithm (type iii update) [11,12] and (iv) overrelaxation updates of the spins at constant configurational energy [13,14]. Each update method is performed in sweeps over the whole lattice and each method (ii), (iii), or (iv) is preceded by a lattice-gas sweep.

The Monte Carlo update algorithms (ii)-(iv), each one preceded by the update (i), are all combined using a hybrid Monte Carlo method [15] in order to reduce correlations between successive configurations in the simulation. After testing different mixtures of the three different algorithms, we found the best sampling was the simple 1 spin-reorientation sweep; 1 Wolff cluster update; 1 overrelaxation sweep, which defines what we will henceforth call a hybrid Monte Carlo step (MCS).

The lattice-gas update attempts to insert a magnetic particle (with a randomly selected spin orientation) at a site where a nonmagnetic one is located or to replace the magnetic particle present at a site by a nonmagnetic one. The acceptance probability is set by the local heat-bath rule

$$p(\Delta E) = 1/[\exp(\Delta E/k_B T) + 1], \tag{2}$$

where ΔE is the change in configurational energy of the proposed move, k_B is the Boltzmann constant (set to unity in our work), and T is the temperature of the system. The single spin-reorientation update is done as in the Metropolis algorithm, but the acceptance probability is also given by the local heat-bath rule [Eq. (2)].

The Wolff update affects only the in-plane components of the spin-1 particles (the z-component is unchanged) in order to obey detailed balance. Analogously, the overrelaxation method is performed with a rotation solely of the in-plane component of the spins in order to keep the configurational energy fixed. The Wolff and the overrelaxation updates are both nonergodic but with the spin-reorientation updates and the lattice gas moves included, the combined algorithm will be ergodic.

For each lattice-gas or spin reorientation move, the new spin direction is randomly selected from the even distribution on the unit sphere. The random number generator used is the routine RAN2 [16].

The system is characterized by two order parameters, the in-plane magnetization per site (m_{xy}) and the concentration of ^{3}He (nonmagnetic) particles (x_3)

$$m_{xy} = \frac{1}{L^3}\left[\left(\sum_i^{L^3} S_i^x\right)^2 + \left(\sum_i^{L^3} S_i^y\right)^2\right]^{1/2}, \tag{3}$$

$$x_3 = \frac{1}{L^3}\sum_i^{L^3}[1 - S_i^2], \tag{4}$$

where L is the linear size of the simple cubic lattice studied. We also computed other relevant thermodynamic quantities as the specific heat c_v, the in-plane component χ_{xy} of the magnetic susceptibility and the concentration susceptibility χ_{conc}

$$c_v = L^3 \frac{\langle E^2\rangle - \langle E\rangle^2}{T^2}, \tag{5}$$

$$\chi_{xy} = L^3 \frac{\langle m_{xy}^2\rangle - \langle m_{xy}\rangle^2}{T}, \tag{6}$$

$$\chi_{\text{conc}} = L^3 \frac{\langle x_3^2\rangle - \langle x_3\rangle^2}{T}, \tag{7}$$

where E is the energy per spin and T the temperature of the system.

The global phase diagram has been obtained through the location of the maximum of the specific heat and of the in-plane magnetic susceptibility. We have considered finite $L\times L\times L$ lattices with periodic boundary conditions. To locate the maximum we performed preliminary simulations for each value of the parameters used, with a temperature step $\Delta T = 0.1$ and runs comprising up to 10^4 MCS after equilibration. Once we obtained the approximate location of the maximum from this preliminary simulation, we performed another one in the vicinity of the peak using $\Delta T = 0.01$ with runs comprising now up to 4×10^4 MCS. This procedure has been done considering just a particular finite lattice, namely, $L=10$. However, we have also done a finite-size scaling analysis [17,18] at some specific points in the vicinity of the tricritical point by taking $10 \leqslant L \leqslant 30$ for second-order transitions and $10 \leqslant L \leqslant 24$ for first-order transitions and using the single bidimensional histogram reweighting technique [19,20]. In this case the histograms have been taken with 10^6 MCS (after equilibration) and from this approach we were able to obtain a more precise value for the transition temperatures.

The main feature of the phase diagram of ^{3}He—^{4}He mixtures is the presence of a tricritical point, and its location was obtained taking into account that the upper critical dimension for tricriticality is $d_> = 3$. Thus, mean-field theory applies and the probability distribution for the magnetic order parameter takes the Landau form

$$P(m) = P_0 m \exp(-Am^2 - Bm^4 - Cm^6), \tag{8}$$

where $m = |m_{xy}|$ is the modulus of the in-plane magnetization per spin. The parameters P_0, A, B, and C are constants, so that C is always positive and $A = B = 0$ at the tricritical point [10]. The scaling function for Δ_t and T_t are, respectively [10],

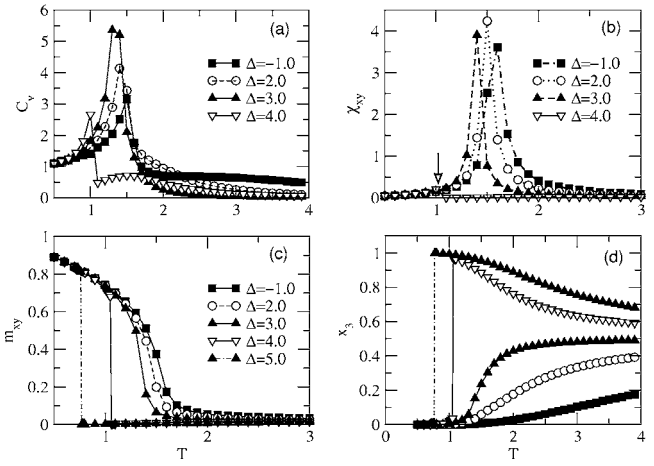

FIG. 1. Behavior of (a) specific heat, (b) in-plane magnetic susceptibility, (c) in-plane magnetization, and (d) concentration of ^{3}He particles as a function of temperature for various values of Δ for $K=1$ and $L=10$. In (b) the arrow indicates the position of the first-order peak for $\Delta=4.0$. The error bars are of the same order as the symbol sizes. The legend in (c) applies also to (d).

$$\Delta_t(L) = \Delta_t + \frac{\delta_1}{L} + \frac{\delta_2}{L^2},$$

$$T_t(L) = T_t + \frac{t_1}{L} + \frac{t_2}{L^2}, \tag{9}$$

where $\Delta_t(L)$ and $T_t(L)$ are the coordinates of the finite-size tricritical points and δ_1, δ_2, t_1, t_2 are fit parameters used to locate the tricritical point (Δ_t, T_t) at the thermodynamic limit.

IV. RESULTS

A. $K=1.0$

The behavior of the specific heat, in-plane magnetic susceptibility, in-plane magnetization and the concentration of ^{3}He particles as a function of temperature is shown in Fig. 1 for $K=1.0$ and various values of the parameter Δ. All results refer to $L=10$. The specific heat, Fig. 1(a), and the in-plane magnetic susceptibility, Fig. 1(b), both display a sharp peak which shifts towards lower temperatures as Δ increases (for $\Delta=4.0$, the peak in the in-plane susceptibility is very small and its location is indicated by an arrow). The in-plane magnetization [Fig. 1(c)] displays a pronounced jump for $\Delta \geqslant 4$, which indicates the onset of a first-order phase transition. This is also observed in the behavior of the concentration of ^{3}He particles. Associating these maxima in χ_{xy} and c_v to the phase transitions, we are able to plot the phase diagram for the model as in Fig. 2. For Δ below the tricritical point, the system undergoes a second-order phase transition (the lambda transition) from a superfluid ^{4}He-rich phase to a normal phase as the temperature increases. For values of Δ above the tricritical point, the second-order transition is preempted by a first-order transition, separating the superfluid ^{4}He-rich phase from the normal phase. The extension of the first-order transition line for lower temperatures is quite difficult to be obtained from the simulations performed. The concentration of ^{3}He in the normal phase varies depending on the region of the phase diagram. For $\Delta < \Delta_t$, the system presents a ^{4}He-rich, normal phase, but the concentration of ^{3}He atoms gradually increases as the system approaches the tricritical point, so that a ^{3}He-rich, normal phase takes the scene.

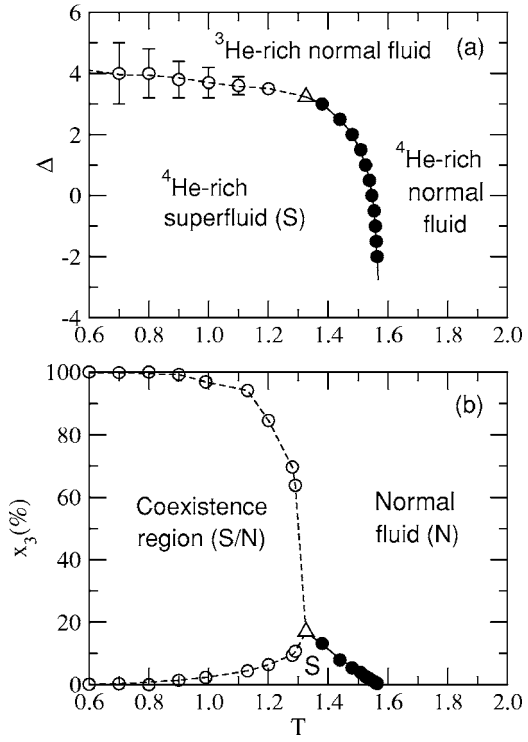

FIG. 2. Phase diagram of the model (a) in the Δ-T and (b) in the temperature-concentration (x_3) planes for $K=1$ and $L=10$ [in (b) we have chosen x_3 versus T for an easier comparison with (a)]. The tricritical point (open triangle) is located at $[\Delta_t, T_t] = [3.230(5), 1.3257(9)]$. Open circles (dashed line) represent first-order transitions and, full circles (full line), second-order transitions. The lines are only guides to the eyes. When not indicated, the error bars are the same size as the symbols or smaller.

The corresponding phase diagram in the temperature-concentration plane is also shown in Fig. 2. The phase diagram obtained qualitatively reproduces the experimental one for ^{3}He—^{4}He mixtures. The tricritical ^{3}He concentration is, however, small ($x_3 \approx 17\%$) when compared to the one obtained experimentally (67%) [6].

The tricritical point, as mentioned in the previous section, was found by the study of the probability distribution for the magnetic order parameter. The basic idea in obtaining the tricritical point is to walk along the second-order transition line, varying Δ and T, and to probe the magnetic order parameter distribution along the way until we find the point where $P(m)$ displays the appropriate shape, with $A=B=0$ [see Eq (8)]. In practice, we set $A=B=0$ in the fitting function and used P_0 and C as fitting parameters. The tricritical point is achieved when we get a visually satisfactory fit with the lowest possible value for the merit function χ^2. The error is estimated by assessing the region where changing the values of the coordinates Δ_t and T_t of the estimated tricritical

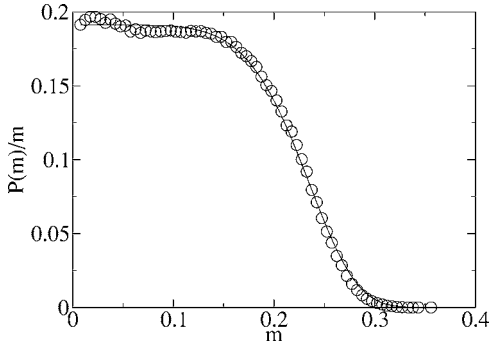

FIG. 3. Probability distribution of the magnetic order parameter for L=30 at $[\Delta_t(30), T_t(30)]=[3.2935(5), 1.3014(2)]$. The solid line is the least square fit to the data, according to Eq. (8), with $A=B=0$.

point does not sensitively affect the obtained minimum χ^2.

The search for the tricritical point was facilitated by the use of bidimensional histograms, which allowed us to re-weight simultaneously in both Δ and T. From a single simulation at a point close to the transition line we were able to obtain several other points along this line. A new simulation became necessary only when the re-weighting was no longer reliable. Thus, for each lattice size L a pseudotricritical point $[\Delta_t(L), T_t(L)]$ was found following the criteria described above. Performing finite-size scaling analysis for $\Delta_t(L)$ and $T_t(L)$ we were able to obtain the tricritical point for $L \to \infty$. The assumed Landau form describes rather accurately the probability distribution $P(m)$ as it can be seen in Fig. 3. The finite-size scaling results for $\Delta_t(L)$ and $T_t(L)$ are shown in Fig. 4. From this study we conclude that the tricritical point is located at $[\Delta_t, T_t]=[3.1313(4), 1.293(1)]$.

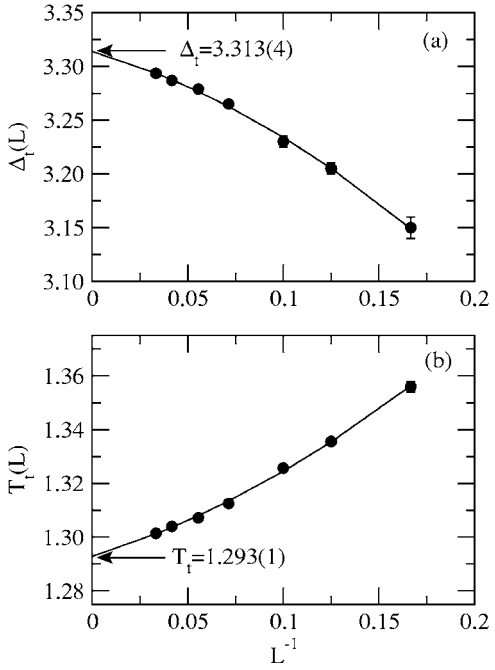

FIG. 4. Finite-size scaling for the parameters (a) Δ_t and (b) T_t at the tricritical point. The solid line is the least-square fit to the data according to Eq. (9).

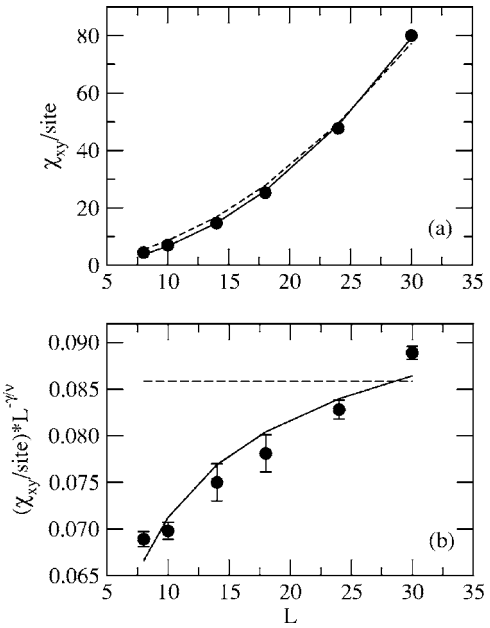

FIG. 5. Finite-size scaling analysis for the maximum of the in-plane magnetic susceptibility at tricriticality; (a) results for $\chi_{xy}/site$; (b) analysis for $(\chi_{xy}/site)\times L^{-\gamma/\nu}$. The solid line corresponds to the least-square fit with the logarithmic correction, while the dashed line is the fit without the logarithmic correction. When not shown, error bars are smaller than the symbol sizes.

We also investigated the finite-size behavior of the in-plane magnetic susceptibility at tricriticality (Fig. 5). The maximum of the susceptibility obtained at the pseudotricritical point as a function of the lattice size L agrees very well with the predicted scaling function [10,21]

$$\chi = \chi_0 \left(\frac{L}{l_0}\right)^{\gamma/\nu} \left(\ln \frac{L}{l_0}\right)^{1/4} \tag{10}$$

but the logarithmic correction is important. This is clearly observed in Fig. 5(b), where we see that multiplying χ_{xy} by $L^{-\gamma/\nu}$ does not yield a straight horizontal line. A curve still remains, which is reasonably fitted by a logarithmic function. A better fit would be expected if enough larger lattice sizes were used (here we only accessed the initial tail of the logarithmic function). In this analysis, $\gamma/\nu=2$, the expected value for the tricritical point.

A more precise picture of the phase diagram is shown in Fig. 6, where some points in the vicinity of the tricritical point are depicted for $L \to \infty$. The points shown were obtained using histogram reweighting and finite-size scaling analysis. The scaling behavior for the temperature for each of the transition points are displayed in Fig. 7, where we used the expected values for the respective exponents for the first- and second-order transition lines, which are the dimension of the system (first-order) and $\nu_{xy}=0.669$ [3] for the three-dimensional XY model (second-order).

From histogram reweighting we were able to obtain the probability distribution of the magnetic order parameter m_{xy} at the transition temperature. This was also used to corroborate the order of the phase transition. The first-order transi-

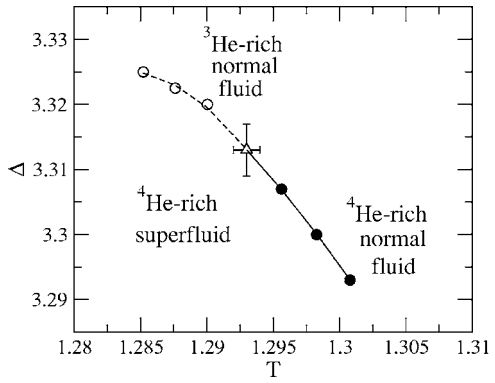

FIG. 6. Phase diagram in the vicinity of the tricritical point (open triangle). The points shown were obtained for $L\to\infty$. The open circles (dashed line) refer to first-order phase transitions and, the full circles (full line), to second-order phase transitions. The lines are only guides to the eyes and the error bars are smaller than the symbol sizes, except for the tricritical point.

tion is characterized by a bimodal probability distribution, while a single-peaked distribution characterizes a second-order transition (Fig. 8). This analysis of $P(m)$ was important not only to characterize the order of the phase transition but also to assess the accuracy of the histogram reweighting performed.

B. $K<1$

We also studied the phase diagram for $K=0$ and $K=-1$, using $L=10$, as shown in Fig. 9. The results obtained led us to conclude that, in the range $-1.0\leqslant K\leqslant 1.0$, the phase diagram of the model satisfactorily reproduces the topology of the phase diagram for ^{3}He—^{4}He mixtures. It is interesting to observe that, for all values of K studied, as Δ decreases, the critical temperature of the system tends to that of the 3D *XY* model. This behavior is expected, since the smaller the value of Δ, the greater the value of the chemical potential μ_4 for ^{4}He relatively to μ_3, what tends to suppress the occurrence of ^{3}He (nonmagnetic) particles. It is also worth observing that the reduction of the value of the parameter K induced a noticeable change in the tricritical temperature and also in the tricritical concentration of ^{3}He particles, so that these parameters at tricriticality could be brought to a better accordance with the experimental values (see Table I). The temperature T on this table is shown as a ratio of T/T_S, where T_S is the temperature of the superfluid transition for pure ^{4}He (used for the experimental ratio, given by $T/T_S=0.4$ [10]), which is equivalent to the critical temperature of the 3D *XY* model [$T_c^{-1}=0.64440(5)$ [3], used for the theoretical ratios]. The tricritical point for $K=-1.0$ and $K=0$ was estimated extending the first- and second-order transition lines close enough one to each other. The approximate location was then given by $[\Delta_t,T_t]=[(\Delta_1+\Delta_2)/2,(T_1+T_2)/2]$, where the index 1 (2) refers to the terminal point obtained for the first (second)-order line in each case. The estimated location for the tricritical point for $K=-1.0$ is thus $[\Delta_t,T_t]=[-3.6(1),0.74(4)]$ and, for $K=0$, $[\Delta_t,T_t]=[0.6(1),0.83(3)]$.

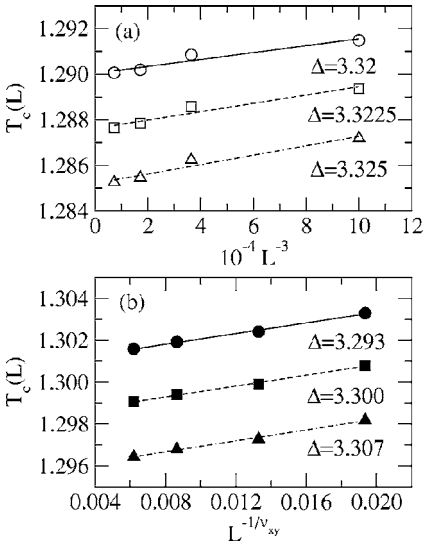

FIG. 7. Finite-size scaling analysis for the transition temperatures on the (a) first- and (b) second-order transition lines in the vicinity of the tricritical point. The lines are the least-square fit to the data. The error bars are smaller than the size of the symbols.

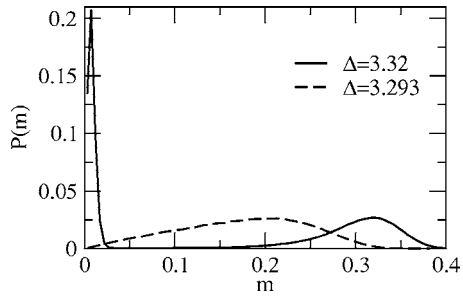

FIG. 8. Probability distribution for the in-plane magnetization for the first ($[\Delta,T]=[3.32,1.29145]$, full line) and second-order ($[\Delta,T]=[3.293,1.30190]$, dashed line) transitions ($L=24$).

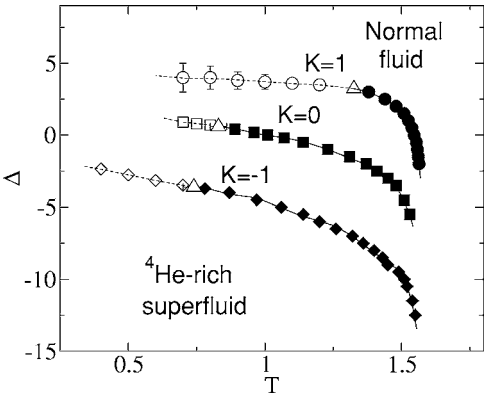

FIG. 9. Phase diagram for $L=10$ and different values of the parameter K. The open symbols (dashed lines) refer to first-order phase transitions and full symbols (full lines), to second-order transitions. The tricritical point for each value of K is indicated by an open triangle. The second-order transition lines extend towards the critical temperature of the three-dimensional *XY* model, when $\Delta\to-\infty$ (see text). The lines are only guides to the eyes.

TABLE I. ^{3}He concentration and temperature at tricriticality for different values of K for the VBEG model. The values for $K=1$ are the estimates for the thermodynamic limit. For $K=0$ and $K=-1.0$, the results refer to $L=10$.

	$x3(\%)$	T/T_S
Experimental	67	0.4
$K=1.0$	18(2)	0.8332(7)
$K=0.0$	40(8)	0.53(2)
$K=-1.0$	35(8)	0.48(4)

C. $K=1.3$

The scenario, however, dramatically changes for $K \gtrsim 1$, for instance $K=1.3$. The tricritical point disappears and now the second-order line ends at a critical endpoint on the first-order line, which extends itself until its extinction at a double critical endpoint [22] (Fig. 10). The approximate location of the critical endpoint is $[\Delta_{CE}, T_{CE}]=[4.18(5), 1.42(1)]$, which can be easily obtained by extending the second-order line very close to the first-order one. The location of the double critical endpoint, however, is not so straightforward, but it can be determined with good precision through the study of the probability distribution associated with the order parameter. Note that similar phase boundary structures have been predicted by mean field theory. They have been, however, notoriously difficult to observe in simulations [23,24]. It is known that each universality class is characterized by a set of scaling functions, so that systems belonging to the same universality class present the same scaling functions [25,26]. Thus, if we know a priori the universality class of the critical point we want to locate, we can walk along the first-order line and probe the probability distribution until we find the point with the expected universal behavior. In fact, this is the case for the critical point considered here. In the region of the phase diagram where we have only normal fluid (see Fig. 10), the order parameter is essentially the concentration of ^{3}He (or ^{4}He) particles and the system behaves as a three-dimensional *lattice gas*, which is in the three-dimensional Ising universality class. In this case, the corresponding probability distribution has been already computed through extensive Monte Carlo simulations [27].

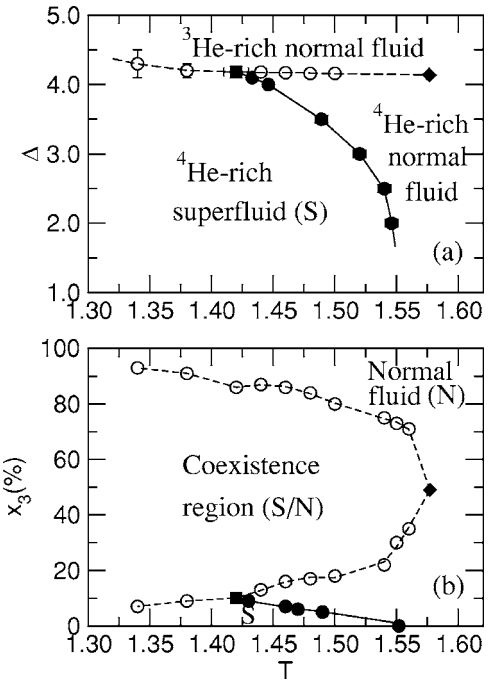

FIG. 10. Phase diagram (a) in the Δ-T and (b) in the concentration-temperature planes for $L=10$ and $K=1.3$. The open circles (dashed line) refer to first-order transitions and, the full symbols (full line), to second-order transitions. The critical endpoint is represented by a full square and, the double critical endpoint, by the full diamond. The lines are only guides to the eyes. When not indicated, the error bars are smaller than the symbol sizes.

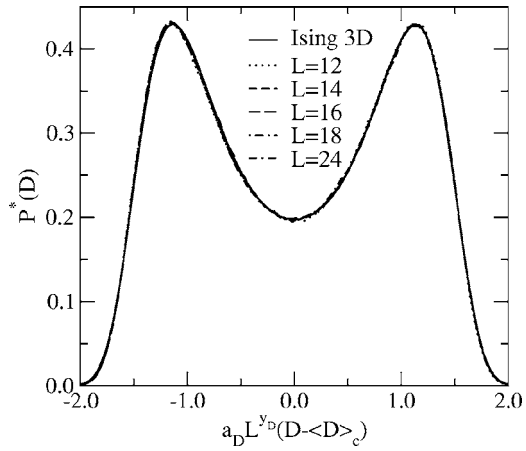

FIG. 11. Universal probability distribution for the double critical endpoint ($K=1.3$).

Due to the lack of symmetry between the phases involved we were led to employ field-mixing theory [28,29] in order to study the order parameter probability distribution. The critical point in the T-Δ plane is controlled by two relevant scaling fields τ and δ, which are linear combinations of the thermodynamic fields T and Δ

$$\tau = T - T_c + s(\Delta - \Delta_c),$$

$$\delta = \Delta - \Delta_c + r(T - T_c), \tag{11}$$

where Δ_c and T_c are the field values at the critical point, and r and s control the degree of field mixing.

The conjugate scaling operators $\mathcal{E}$ and $\mathcal{D}$ are also linear combinations of the nearest-neighbor energy E and the quadrupole term Q

$$\mathcal{E} = \frac{E - rQ}{1 - rs},$$

$$\mathcal{D} = \frac{Q - sE}{1 - rs}, \tag{12}$$

where $E=\Sigma_{\langle i,j\rangle}[S_i^x S_j^x + S_i^y S_j^y]$ and $Q=\Sigma_i S_i^2$. According to finite-size scaling [28] and renormalization group procedures [30], the probability distribution $P_L(\mathcal{E}, \mathcal{D})$ at criticality is given by

TABLE II. Parameters for the $P_L^*(D)$ distribution. The best estimate for the location of the double critical endpoint is $T_c=1.5745(2)$ and $\Delta_c=4.13899(4)$.

L	T	Δ	s
12	1.5759(1)	4.13883(1)	−0.1(1)
14	1.5755(1)	4.13885(1)	−0.1(1)
16	1.5752(1)	4.13889(1)	−0.1(1)
18	1.5750(1)	4.13888(1)	−0.1(1)
24	1.5747(1)	4.13899(1)	−0.1(1)

$$P_L(\mathcal{E},\mathcal{D}) \simeq \Lambda_{\mathcal{E}}^{+}\Lambda_{\mathcal{D}}^{+}P^{*}(\Lambda_{\mathcal{E}}^{+}\delta\mathcal{E},\Lambda_{\mathcal{D}}^{+}\delta\mathcal{D}), \tag{13}$$

$$\Lambda_{\mathcal{E}} = a_{\mathcal{E}}L^{d-y_{\mathcal{E}}}, \Lambda_{\mathcal{D}} = a_{\mathcal{D}}L^{d-y_{\mathcal{D}}} \tag{14}$$

where $\Lambda_{\mathcal{E}}\Lambda_{\mathcal{E}}^{+}=\Lambda_{\mathcal{D}}\Lambda_{\mathcal{D}}^{+}=L^d$ and $\delta\mathcal{E}=\mathcal{E}-\langle\mathcal{E}\rangle_c$ and $\delta\mathcal{D}=\mathcal{D}-\langle\mathcal{D}\rangle_c$. The probability distribution P^* is a universal function, characteristic of a definite universality class. Moreover, $P_L(\mathcal{E},\mathcal{D})$, given in Eq. (13), is related to the joint probability distribution $P_L(E,Q)$ through

$$P_L(E,Q) = \frac{1}{1-rs}P_L(\mathcal{E},\mathcal{D}). \tag{15}$$

Formal integration of $P_L(\mathcal{E},\mathcal{D})$ over $\mathcal{E}$ yields $P_L(\mathcal{D})$, which is the desired distribution, since $\mathcal{D}$ is the conjugate scaling operator of the corresponding scaling field δ. Choosing the nonuniversal factor $a_{\mathcal{D}}$ so that the distribution $P_L(\mathcal{D})$ as a function of $a_{\mathcal{D}}L_{\mathcal{D}}^{y}(\mathcal{D}-\langle\mathcal{D}\rangle_c)$ has unit variance, we obtain the universal probability distribution P_L^*, which depends only on three parameters T, Δ, and s. Thus, by tuning T, Δ, and s, with the aid of the histogram technique, we can collapse $P_L^*(D)$, for various lattice sizes, over the previously computed universal distribution of the three-dimensional Ising model. Performing simulations with $3-10\times10^6$ MCS for lattices $L\leqslant24$, we now store a table of E and Q from which we obtain the distribution $P_L(\mathcal{D})$. We could then obtain the values for the parameters T, Δ, and s for each lattice size L at the critical point considered. The collapsed probability distributions are shown in Fig. 11 and the values of the parameters for each lattice size are shown in Table II.

The finite-size scaling analysis for the critical temperature is shown in Fig. 12, where we used the appropriate exponents $\nu=0.629$ and $\theta=0.54$ for the three-dimensional Ising model [31]. The critical temperature at the thermodynamic limit is $T_c=1.5745(2)$. The value for Δ_c is given by 4.13899(4).

V. CONCLUSIONS

The phase diagram for the *XY* version of the Vector Blume-Emery-Griffiths model was studied by means of Monte Carlo simulations. This model satisfactorily reproduces the topology of the phase diagram for ^{3}He—^{4}He mixtures for $-1.0\leqslant K\leqslant1.0$. The phase diagram displays a second-order transition line isolated from a first-order transition line by a tricritical point. For Δ below the tricritical point, the system exhibits a superfluid, ^{4}He-rich phase which undergoes a second-order transition to a ^{4}He-rich, normal phase. For values of Δ above the tricritical point, the superfluid ^{4}He-rich phase undergoes a first-order transition to a normal phase, whose concentration of ^{3}He gradually increases as the system moves away from the tricritical point. For $K\gtrsim1$, for instance, $K=1.3$, the phase diagram changes substantially. The tricritical point disappears and the second-order line ends at a critical endpoint on the first-order line, which extends until a double critical endpoint, located with good precision. It is worth noting that the results obtained for the *XY* version of the VBEG model are qualitatively similar to those obtained by Maciolek *et al.* [10] for the planar rotator version, but not quantitavely. For instance, the tricritical point obtained ($K=1$) for the planar rotator version by Monte Carlo simulations is given by $T_t/T_s=0.744$, while we obtained $T_t/T_s=0.8332(7)$. We also expect that, for different values of K, a third type of phase diagram, displaying a triple point (as predicted by mean field), should also occur. The results obtained will be useful for our subsequent work on dynamic properties of ^{3}He—^{4}He mixtures.

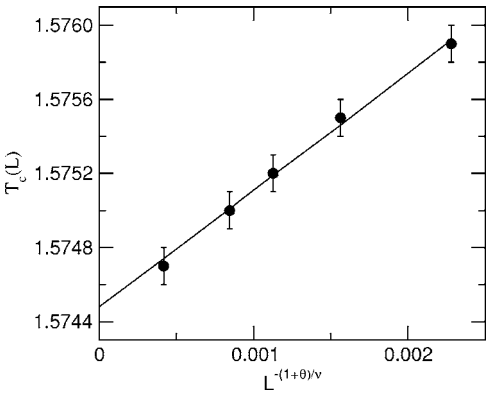

FIG. 12. Finite-size scaling analysis for the double critical endpoint at the end of the first-order transition line ($K=1.3$). The values used for the exponents θ and ν are, respectively, 0.54 and 0.629, the appropriate ones for the three-dimensional Ising model.

ACKNOWLEDGMENTS

We are grateful for fruitful discussions with Shan-Ho Tsai. R.T.S.F. and J.A.P also thank the Center of Simulational Physics at the University of Georgia for its hospitality. R.T.S.F also acknowledges financial support from CNPq-Brazil. This work was funded by CIAM-CNPq Process Grant No. 49.0101/03-8, NASA Grant No. NNC04GB24 and NSF Grants Nos. DMR-0341874 and DMR-0307082.

[1] J. A. Lipa, D. R. Swanson, J. A. Nissen, T. C. P. Chui, and U. E. Israelsson, Phys. Rev. Lett. **76**, 944 (1996).
[2] T. Matsubara and H. Matsuda, Prog. Theor. Phys. **16**, 569 (1956).
[3] M. Krech and D. P. Landau, Phys. Rev. B **60**, 3375 (1999).
[4] K. Nho and E. Manousakis, Phys. Rev. B **64**, 144513 (2001).
[5] E. H. Graf, D. M. Lee, and John D. Reppy, Phys. Rev. Lett. **19**, 417 (1967).
[6] H. A. Kierstead, J. Low Temp. Phys. **35**, 25 (1979).
[7] M. Blume, J. V. Emery, and R. B. Griffiths, Phys. Rev. A **4**, 1071 (1971).
[8] A. N. Berker and D. R. Nelson, Phys. Rev. B **19**, 2488 (1979).
[9] J. L. Cardy and D. J. Scalapino, Phys. Rev. B **19**, 1428 (1979).
[10] A. Maciolek, M. Krech, and S. Dietrich, Phys. Rev. E **69**, 036117 (2004).
[11] U. Wolff, Phys. Rev. Lett. **62**, 361 (1989).
[12] M. E. J. Newman and G. T. Barkema, *Monte Carlo Methods in Statistical Physics* (Clarendon, Oxford, 1999).
[13] M. Creutz, Phys. Rev. D **36**, 515 (1987).
[14] S. G. Pawig and K. Pinn, Int. J. Mod. Phys. C **9**, 727 (1998).
[15] J. A. Plascak, A. M. Ferrenberg, and D. P. Landau, Phys. Rev. E **65**, 066702 (2002).
[16] W. H. Press, S. A. Teukolsky, and W. T. Vetterling, *Numerical Recipes in Fortran 77*, 2nd ed. (Cambridge University Press, New York, 1992), Vol. 1.
[17] *Finite-Size Scaling and Numerical Simulations*, edited by V. Privman (World Scientific, Singapore, 1990).
[18] K. Binder and D. P. Landau, Phys. Rev. B **30**, 1477 (1984).
[19] A. M. Ferrenberg and R. H. Swendsen, Phys. Rev. Lett. **61**, 2635 (1988); A. M. Ferrenberg, *Computer Simulation Studies in Condensed Matter Physics III*, Vol. 53 of *Springer Proceedings in Physics* (Springer-Verlag, Heidelberg, 1991).
[20] D. P. Landau and Kurt Binder, *A Guide to Monte Carlo Simulations in Statistical Physics* (Cambridge University Press, Cambridge, 2000).
[21] D. Lawrie and S. Sarbach, in *Phase Transitions and Critical Phenomena*, edited by C. Domb and J. L. Lebowitz (Academic, London, 1984), Vol. 9.
[22] While this has historically sometimes been termed a "bicritical endpoint," this termination of the two lines of critical points in the extended space of thermodynamic fields is more properly termed a "double critical endpoint" [M. E. Fisher (private communication)].
[23] H. J. Herrmann, E. B. Rasmussen, and D. P. Landau, J. Appl. Phys. **53**, 7994 (1982).
[24] J. D. Kimel, S. Black, P. Carter, and Y.-L. Wang, Phys. Rev. B **35**, 3347 (1987).
[25] K. Binder, Z. Phys. B: Condens. Matter **43**, 119 (1981).
[26] P. H. L. Martins and J. A. Plascak, Braz. J. Phys. **34**, 433 (2004).
[27] M. M. Tsypin and H. W. J. Blöte, Phys. Rev. E **62**, 73 (2000).
[28] N. B. Wilding, A. D. Bruce, J. Phys.: Condens. Matter **4**, 3087 (1992).
[29] J. A. Plascak and D. P. Landau, Phys. Rev. E **67**, 015103(R) (2003).
[30] A. D. Bruce, J. Phys. C **14**, 3667 (1981).
[31] Nigel B. Wilding, Phys. Rev. E **52**, 602 (1995).